Chemical Science

ROYAL SOCIETY OF CHEMISTRY

EDGE ARTICLE

View Article Online
View Journal | View Issue

Cite this: *Chem. Sci.*, 2024, **15**, 4853

All publication charges for this article have been paid for by the Royal Society of Chemistry

Received 19th December 2023
Accepted 12th February 2024

DOI: 10.1039/d3sc06810b

rsc.li/chemical-science

Construction of an $Au_{12}Cd_2$ nanocluster with circularly polarized luminescence by a metal- and ligand-exchange strategy†

Jun Zhou,‡[a] Xiaofei Yang,‡[a] Peisen Zheng,‡[a] Qinzhen Li,[a] Xiaowu Li,[a] Jinsong Chai,[a] Baoyu Huang,*[b] Sha Yang*[a] and Manzhou Zhu*[a]

Excellent luminescence properties and unique chiral structures enable nanoclusters to be a novel class of circularly polarized luminescence (CPL) materials, and their precise structures facilitate the clarification of structure–activity relationships. However, efficiently preparing nanoclusters with CPL properties is still a great challenge. In this work, the luminescent properties as well as the molecular symmetry were simultaneously manipulated to transform the centrosymmetric $Au_{14}Cd_1$ into a chiral $Au_{12}Cd_2$ nanocluster, which has CPL properties. In detail, Cd doping and chiral-ligand exchange were performed simultaneously on the $Au_{14}Cd_1$ nanocluster to realize its photoluminescence enhancement and chiral-framework construction by increasing the alloying degree which is defined as deep-alloying and chiral ligand induction at the same time, resulting in the formation of an $Au_{12}Cd_2$ nanocluster with CPL properties. Further investigations revealed an increased alloying degree in the structure-maintained M_6 kernel of $Au_{12}Cd_2$, which results in a 15-fold enhancement in quantum yield.

Introduction

Fluorescent nanoclusters are of significant interest owing to their ultra-small size, good biocompatibility, and excellent photostability.[1–3] More importantly, their precise structures offer promise for the development of functional materials with interesting optical properties.[4–7] Circularly polarized luminescence (CPL) originates from the chiral emissive states of luminescent materials, which requires an efficient synergy between luminescence and chirality.[8–11] As it can eliminate the interference of achiral materials such as mirror image or racemization, CPL greatly improves the utilization of incident light, thus displaying a more sensitive resolution as a molecular-level sensor.[12–14] Therefore, CPL nanoclusters have a wide range of application prospects in biological probes,[15,16] three-dimensional displays,[17,18] information storage and processing,[19,20] CPL lasers,[21,22] *etc.* The current research focus is on how to highly efficiently prepare circularly polarized luminescent nanoclusters which display both high dissymmetry factor (g_{lum}) and quantum yield (QY).

To address the above issues, the key is to develop an effective strategy to overcome the apparent trade-off between g_{lum} and QY. To construct nanoclusters with CPL properties, the current mainstream strategies include two ways, inducing a chiral factor to a fluorescent nanocluster[23,24] or functionalizing chiral clusters with fluorophores.[25,26] However, these strategies are limited by the fact that most of the nanoclusters are neither chiral nor fluorescent. Given that the atomically precise structure of nanoclusters can be tailored or modified, the implementation of both chiral and fluorescent properties on one nanocluster is expected to be an efficient way to construct nanoclusters with CPL.[27–34] To construct a CPL nanocluster, heterometal doping is expected to be an effective way to enhance the fluorescence properties of a certain nanocluster while maintaining its internal structure in view of the ability of metal doping in influencing the transition dipole.[35,36] On the other hand, the strategy of introducing chiral ligands to construct nanoclusters with optical chirality has been well established, and the major issue remains in the selection of chiral ligands that facilitate the crystallization of nanoclusters.[37,38] In general, it is expected that the CPL properties can be introduced in the clusters in one step by the simultaneous introduction of the heterometal atom and chiral ligand.

Herein, $Au_{14}Cd_1(SR)_{12}$ recently prepared by our group[39] is considered as the precursor for constructing CPL nanoclusters

[a]*Department of Chemistry, Centre for Atomic Engineering of Advanced Materials, Key Laboratory of Structure and Functional Regulation of Hybrid Materials of Ministry of Education, Institutes of Physical Science and Information Technology, Anhui Province Key Laboratory of Chemistry for Inorganic/Organic Hybrid Functionalized Materials, Anhui University, Hefei, Anhui 230601, China. E-mail: yangshac@ahu.edu.cn; zmz@ahu.edu.cn*

[b]*Hunan Provincial Key Laboratory of Environmental Catalysis & Waste Recycling, College of Materials and Chemical Engineering, Hunan Institute of Engineering, Xiangtan 411104, China. E-mail: 22164@hnie.edu.cn*

† Electronic supplementary information (ESI) available: Experimental and characterization details and additional figures and tables (Scheme S1, Fig. S1–S38 and Tables S1–S8) offer more details on the nanoclusters. CCDC 2266860 and 2266865. For ESI and crystallographic data in CIF or other electronic format see DOI: https://doi.org/10.1039/d3sc06810b

‡ Jun Zhou, Xiaofei Yang and Peisen Zheng contributed equally to this work.

because relative studies show that its luminescence properties can be regulated by changing the transition dipole moment.[40,41] Given that heterometal doping is an effective strategy to influence transition dipole, continued doping of Cd atoms in $Au_{14}Cd_1(SR)_{12}$ is expected to enhance fluorescence properties. On the other hand, *R*/*S*-fenchylthiol (*R*/*S*-$C_{10}H_{17}SH$, 1,3,3-trimethylbicyclo[2.2.1]heptan-2-thiol), which has a rigid structure similar to the SAdm and S^{t}Bu of $Au_{14}Cd_1(SR)_{12}$,[39] was employed to introduce chirality in $Au_{14}Cd_1(SR)_{12}$. As a result, optically pure chiral $Au_{12}Cd_2$(*R*/*S*-$C_{10}H_{17}S)_{12}$ (abbreviated to $Au_{12}Cd_2$) nanoclusters with CPL properties were obtained. Compared with the $Au_{14}Cd_1$ nanocluster, $Au_{12}Cd_2$ exhibits a higher quantum yield and is optically active because of the addition of chiral ligands. As revealed by the precise structures, compared with that of $Au_{14}Cd_1$, a similar M_6 core with one more Cd doping and different staple motifs was found in $Au_{12}Cd_2$.

Experimental

Chemicals

In the experimental details, all reagents in addition to the thiol ligand were purchased and used without further purification. The reagents in the study including tetrachloroauric(III) acid ($HAuCl_4 \cdot 4H_2O$, ≥99.99% metals basis), cadmium chloride ($CdCl_2 \cdot 2.5H_2O$, ≥98% metals basis), fenchone ($C_{10}H_{16}O$, ≥99%), sodium borohydride ($NaBH_4$, ≥98%), 1-adamantanethiol (HSAdm, ≥98%), and reduced glutathione (GSH, ≥98%) were purchased from Macklin (Shanghai, China). Solvents including toluene, methanol, dichloromethane, and 1,2-dimethoxyethane were HPLC grade and were purchased from Chron Chemicals Company Limited (Chengdu, China).

Transformation and purification of the $Au_{12}Cd_2$(*R*-$C_{10}H_{17}S)_{12}$ and $Au_{12}Cd_2$(*S*-$C_{10}H_{17}S)_{12}$ nanoclusters

Firstly, $Au_{14}Cd_1$ nanoclusters were synthesized by a two-phase ligand exchange method, and crystals formed after 2–3 days of diffusion with dichloromethane and methanol as previously reported.[39] The *R*-Cd-SR complex was then prepared by mixing 200 μL *R*-fenchylthiol and 2 mg $CdCl_2 \cdot 2.5H_2O$ for about 10 minutes at 60 °C. The *R*-Cd-SR complex was obtained and further purified by centrifugation and washing with methanol. 20 mg of $Au_{14}Cd_1$ crystal were dissolved in 5 mL toluene with the addition of 0.5 mg *R*-Cd-SR complex. The transformation process from $Au_{14}Cd_1$ to $Au_{12}Cd_2$(*R*-$C_{10}H_{17}S)_{12}$ was allowed to proceed for about one day. The raw product containing the $Au_{12}Cd_2$ nanocluster was washed with methanol and its purification was performed with thin-layer chromatographic (TLC) plates. The synthesis of the $Au_{12}Cd_2$ nanocluster follows a similar procedure by replacing *R*-fenchylthiol with *S*-fenchylthiol. The single crystal of the $Au_{12}Cd_2$ nanocluster was obtained by diffusing methanol into the toluene solution of the cluster for about 24 hours.

Measurement information

Dichloromethane was used as solvent to dissolve the nanoclusters for UV-vis spectroscopy and a time-dependent UV-vis test was performed using a Metash UV-6000 spectrophotometer. The X-ray photoelectron spectroscopy (XPS) test was performed on an ESCALAB 250 high-performance electron spectroscopy instrument with a monochromatic Al-Kα (1486.8 eV) excitation source. An electrospray ionization mass spectrometry (ESI-MS) test was performed with a Waters Xevo G2-XSQ-TOF mass spectrometer. Single-crystal X-ray diffraction (SCXRD) was carried out on a STOE STADIVARI diffractometer, using graphite-monochromated Cu Kα radiation ($\lambda = 1.54186$ Å). Circular dichroism was analysed on a Biologic MOS-500 spectrophotometer. Tests on photoluminescence including fluorescence quantum yield and fluorescence lifetime were measured on an FL-4500 fluorescence spectrometer with a relative optical density of 0.1. Circularly polarized luminescence properties were measured on a JASCO CPL-300 spectrophotometer. Nuclear magnetic resonance (NMR) spectra were measured using a JEOL JNM-ECZ400S. Gas chromatography-mass spectra (GC-MS) were measured using a Thermo Fisher TSQ8000EVO.

Computational method and details

Both DFT calculations and TDDFT calculations were done using ORCA5.0.2 software.[42] The geometric optimization of the ground and excited states of the clusters was carried out using the PBE[43] exchange–correlation functional and the def2-SV(P) basis set. To improve the computational efficiency, both DFT and TDDFT calculations were performed using the RI (Resolution of Identity) approximation with the auxiliary basis set def2/J.[44] All structures were optimized in the gas phase. The convergence criteria for geometric optimization are set as 1.0×10^{-6} Hartree for energy change and 3.0×10^{-4} Hartree/Å for gradient change, respectively. The geometric optimization of the S_0 is performed by using the DFT method, and the structural optimization of S_1 and S_2 is performed using the TDDFT method. Based on the optimized structure of S_0, the circular dichroism spectra are also calculated at the PBE/def2-SV(P) level. The TD-DFT calculations evaluate the excitation energies of the lowest 500 singlet-to-singlet transitions.

Results and discussion

Synthesis, transformation, and characterization

In this work, the $Au_{14}Cd_1$ nanocluster was selected as a precursor, and was prepared by a two-phase ligand-exchange method described in the previous study.[39] The obtained cluster is dissolved in toluene and reacted with excess *R*/*S*-Cd-SR complex to obtain the targeting nanoclusters. Time-dependent UV-vis spectra were employed to trace the reaction process (Fig. 1a and S8†). As shown in Fig. 1a, $Au_{14}Cd_1$ showed two characteristic absorption peaks located at 414 and 563 nm, respectively. As the reaction proceeded, the absorption peak at 414 nm underwent a blue shift to 408 nm gradually. At the same time, the absorption peak at 563 nm was redshifted and finally changed to 570 nm. The change in absorption peaks implies that the cluster transformation has occurred. TLC was employed on the raw product to confirm the cluster change of the $Au_{14}Cd_1$. It revealed that the $Au_{14}Cd_1$ nanocluster had been transformed into another nanocluster with a yield of about 70% (Fig. S9 and S10†).

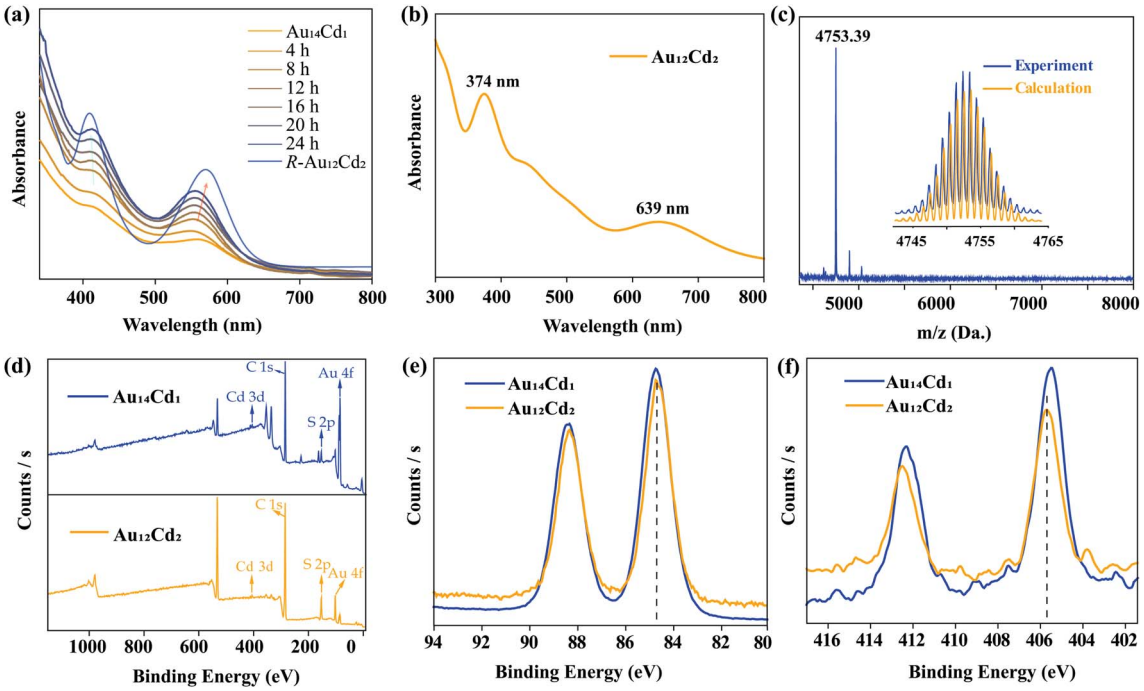

Fig. 1 (a) Time dependent UV-vis spectra tracking the transformation process from $Au_{14}Cd_1$ to *R*-$Au_{12}Cd_2$; (b) calculated UV-vis spectrum of *L*/*R*-$Au_{12}Cd_2$ by DFT; (c) ESI-MS of the *R*-$Au_{12}Cd_2$ nanocluster in CH_2Cl_2, inset shows the experimental and calculated isotopic patterns of $[R\text{-}Au_{12}Cd_2(C_{10}H_{17}S)_{12}Cs]^+$; (d) comparison of the XPS curves of $Au_{14}Cd_1$ and *R*-$Au_{12}Cd_2$ ranging from 0 to 1100 eV; (e) Au 4f peaks of the $Au_{14}Cd_1$ and *R*-$Au_{12}Cd_2$; (f) Cd 3d peaks of the $Au_{14}Cd_1$ and *R*-$Au_{12}Cd_2$.

To further confirm the role of the cadmium atom and the thiol in triggering the transformation reaction, $Au_{14}Cd_1$ was reacted with the Cd atom and the thiol separately. After treatment with $CdCl_2$, the solution of $Au_{14}Cd_1$ became colorless and finally produced a suspension. This result indicated that the addition of a Cd(II) salt alone to the system will lead to the decomposition of $Au_{14}Cd_1$ (Fig. S11†). On the other hand, with the addition of fenchylthiol, $Au_{14}Cd_1$ can also be converted to $Au_{12}Cd_2$ but with a quite low yield and accompanied by the formation of some precipitate. The above results suggest that the thiol plays an important role in inducing the conversion of $Au_{14}Cd_1$, but the combination of the Cd(II) and the thiol can make the transformation more efficient (Fig. S12–S15†). For comparison, two absorption peaks at 408 nm and 570 nm were found in the $Au_{12}Cd_2$ nanocluster, which just shows a slightly red or blue shift to that of $Au_{14}Cd_1$ (414 nm and 563 nm). Further, the origin of the absorption peaks of the $Au_{12}Cd_2$ nanocluster was analyzed with DFT calculations. As shown in Fig. 1b, the experimental UV-vis spectrum has been well reproduced by theoretical calculations. The major orbital contributions of the peak at 639 nm from HOMO → LUMO+1 and other contributions are shown in the ESI (Fig. S16 and Table S1†).

The composition of the transformation products was first determined by ESI-MS and XPS. As shown in Fig. 1c and S17,† an intense peak at 4753.39 Da was found in the ESI-MS spectrum, which can be assigned to the formula of $[Au_{12}Cd_2(C_{10}H_{17}S)_{12}Cs]^+$ (calculated: 4753.58 Da). The isotopic pattern of $[Au_{12}Cd_2(C_{10}H_{17}S)_{12}Cs]^+$ matches well with the calculated one (Fig. 1c and S17,† inset). From Fig. 1d, the full XPS spectrum of $Au_{12}Cd_2$ nanoclusters shows that $Au_{12}Cd_2$ contains the elements of Au, Cd, and S. For comparison, the Au 4f and the Cd 3d binding energies of $Au_{14}Cd_1$ and $Au_{12}Cd_2$ were further characterized to compare the valence states of Au and Cd. As shown in Fig. 1e, both the Au 4f peak of $Au_{14}Cd_1$ and that of $Au_{12}Cd_2$ are located at 84.72 eV, indicating a similar valence state of Au in these two nanoclusters. In addition, the Cd 3d peak of $Au_{12}Cd_2$ has a shift of about 0.2 eV with that of $Au_{14}Cd_1$ (405.75 eV for $Au_{12}Cd_2$ *vs.* 405.55 eV for $Au_{14}Cd_1$, Fig. 1f). This may be due to the two Cd atoms in $Au_{12}Cd_2$ being directly connected to peripheral organic ligands, resulting in the Cd atoms being closer to Cd^{2+} (405.75 eV).[45] Their comparable UV-vis absorption spectra imply that the two nanoclusters may have a comparable electronic structure, which suggests that the basic core framework structure has been maintained.

Crystal structure analysis

X-ray single-crystal diffraction was performed to determine the geometric structure of the $Au_{12}Cd_2$ nanocluster. $Au_{12}Cd_2$ nanoclusters with chiral configurations were named *L*-$Au_{12}Cd_2$ and *R*-$Au_{12}Cd_2$ respectively according to the configurations of their thiolate ligands (Fig. S18 and S19†). As revealed by X-ray crystallography, *L*-$Au_{12}Cd_2$ and *R*-$Au_{12}Cd_2$ crystallized in the orthogonal $P2_12_12_1$ space group (Table S2†) and monoclinic $P2_1$ space group (Table S3†), respectively. The unit cell of both nanoclusters contains four cluster molecules, showing a 4H packing arrangement ($Z = 4$) (Fig. S20 and S21†). For the

structural details of the nanoclusters, $Au_{12}Cd_2$ is composed of twelve Au atoms, two Cd atoms, and 12 fenchylthiol ligands, formulated as $Au_{12}Cd_2(SR)_{12}$. $Au_{12}Cd_2$ contains an Au_4Cd_2 (a twisted octahedron) surrounded by two Au_3S_4 motifs and two Au_1S_2 motifs (Fig. 2a and b).

The geometric structure of the $Au_{12}Cd_2$ nanoclusters can serve as an ideal platform for exploring their chiral origins. Fig. S18 and S19† show a pair of enantiomers of $Au_{12}Cd_2$ nanoclusters. To reveal the chiral origin of the $Au_{12}Cd_2$ nanocluster, we first investigated the core of the $Au_{12}Cd_2$ nanocluster. As shown in Fig. 2c, a pair of chiral Au_4Cd_2 kernels is identified, which has a twisted octahedral configuration. Taking the two cadmium atoms in the kernel as the central axis, the remaining four gold atoms exhibit a significant distortion compared to a standard octahedron *i.e.*, one is left spinning and the other is right spinning. The left one shows a −19.175° distortion angle in the *L*-Au_4Cd_2 kernel, while the right one shows a 20.368° twist in the *R*-Au_4Cd_2 kernel (Fig. 2c). Interestingly, the link between the kernel and the Au_1S_2 motif, which is the M–L surface, inherited the distortion in that direction (Fig. 2d). The above results suggest that in addition to the introduced chiral ligands, the distortion of the core and the M–L interface also contributes to the chirality of the nanoclusters.

Furthermore, the degree of distortion in $Au_{14}Cd_1$ was then compared with that of $Au_{12}Cd_2$. As revealed in Fig. S22,† the structure of the $Au_{14}Cd_1$ nanocluster reveals that the twist angle of the four gold atoms at the center in the core is −2.376°, which is quite different from that of $Au_{12}Cd_2$. Therefore, it can be considered that the degree of chiral torsion has increased during the transformation process, which was caused by the introduction of chiral ligands.[46] The detailed comparison and the structural evolution of the two nanoclusters are shown in Fig. 3. For their peripheral structures, the two Au_4S_5 and one Au_1S_2 motifs in $Au_{14}Cd_1$ were converted into two Au_3S_4 and two Au_1S_2 motifs in the $Au_{12}Cd_2$ *via* the breakage and reorganization of the Au–S bonds. The implementation of this process is mainly dependent on the introduction of foreign ligands and ligand etching. With the breakage of the Au–S bond during the reaction, the Au_5Cd_1 kernel surface can be exposed to proceed with the subsequent Cd doping. This is the deep alloying strategy, where the alloy $Au_{14}Cd_1$ nanocluster is used as a precursor to increase the Cd doping by adding cadmium salts again. An increase in the ratio of Cd to Au atom from 1 : 14 to 1 : 6 was realized. This may reduce the site resistance on the surface of the kernel and increase the chance of collision between the Cd atom and the kernel, thus facilitating Cd doping. So, the thiols play a key role in the conversion from $Au_{14}Cd_1$ to $Au_{12}Cd_2$, while the addition of a cadmium atom would improve the yield by increasing the cadmium concentration of the reaction system.

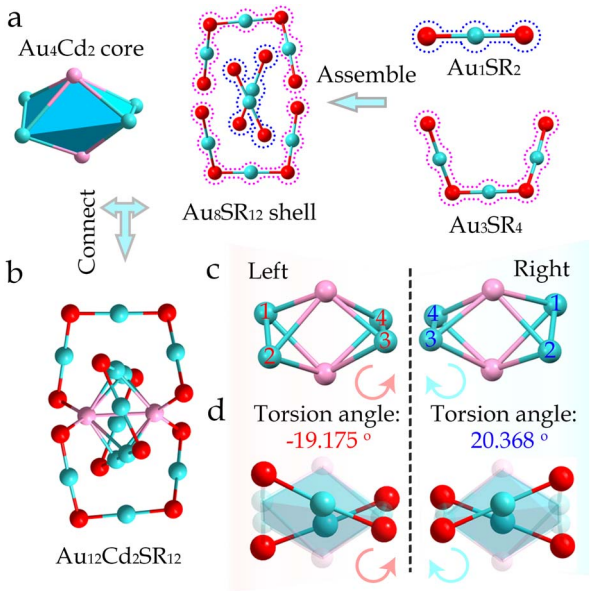

Fig. 2 (a) The detailed structure analysis of the $Au_{12}Cd_2$ showing the Au_4Cd_2 core, two Au_1SR_2 motifs and two Au_3SR_4 motifs; (b) total structural framework of $Au_{12}Cd_2(SR)_{12}$; (c) the torsion angle core of $Au_{12}Cd_2$ (the torsion angle is the angle between the plane of Au_1-Au_2Au_3 and that of $Au_2Au_3Au_4$), (d) the link between the core and the Au_1S_2 motif in the *L*-configuration (left) and *R*-configuration (right). (Color labels: blue = Au, pink = Cd, red = S, all the C and H atoms have been omitted for clarity).

Study of optical properties

Since the chiral factor has been introduced into the $Au_{12}Cd_2$ nanoclusters and its transition dipole moment was also regulated by increasing the doping degree of heteroatoms, a series of tests related to chirality, fluorescence, and circularly polarized luminescence of this cluster were performed. The fluorescence change was focused firstly, and a significant enhancement of fluorescence was found in $Au_{12}Cd_2$ when compared with that of $Au_{14}Cd_1$. As shown in Fig. 4a, $Au_{12}Cd_2$ shows emission peaks at around 720 and 820 nm under the excitation at 408 nm. The fluorescence intensity of *R*-$Au_{12}Cd_2$ was nearly fifteen times higher than that of $Au_{14}Cd_1$ with the same concentration (Fig. 4a) and the absolute quantum yields were measured to be 0.18% for $Au_{14}Cd_1$ and 2.7% for *R*/*L*-$Au_{12}Cd_2$. Both $Au_{14}Cd_1$ and $Au_{12}Cd_2$ were revealed to exhibit two-component lifetime, that is, $\tau_1 = 3.756 \times 10^{-10}$ s and $\tau_2 = 5.102 \times 10^{-9}$ s for $Au_{14}Cd_1$, $\tau_1 = 3.844 \times 10^{-10}$ s and $\tau_2 = 4.439 \times 10^{-9}$ s for *R*-$Au_{12}Cd_2$, and $\tau_1 = 1.582 \times 10^{-10}$ s and $\tau_2 = 4.162 \times 10^{-9}$ s for *L*-$Au_{12}Cd_2$ (Fig. 4b, S23 and S24†).

DFT calculations were employed to further reveal the fluorescence origin of the nanoclusters (Fig. S25 and Tables S4–S6†). The DFT results show that the introduction of Cd atoms in the core plays a more significant role in increasing the fluorescence intensity of the nanoclusters. The enhanced fluorescence performance of $Au_{12}Cd_2$ is caused by the combination of Cd atom doping and chiral ligand modification. However, the main factor that improves the fluorescence properties of $Au_{12}Cd_2$ is the doping of Cd atoms into the core. As the two PL peaks both originate from the core-based HOMO–LUMO+1 transition, there is no obvious difference between the PL excitation spectra corresponding to PL at 720 nm and 820 nm.[42] This result indicates that the doping of the second Cd atom in the core is beneficial to the improvement of its fluorescent

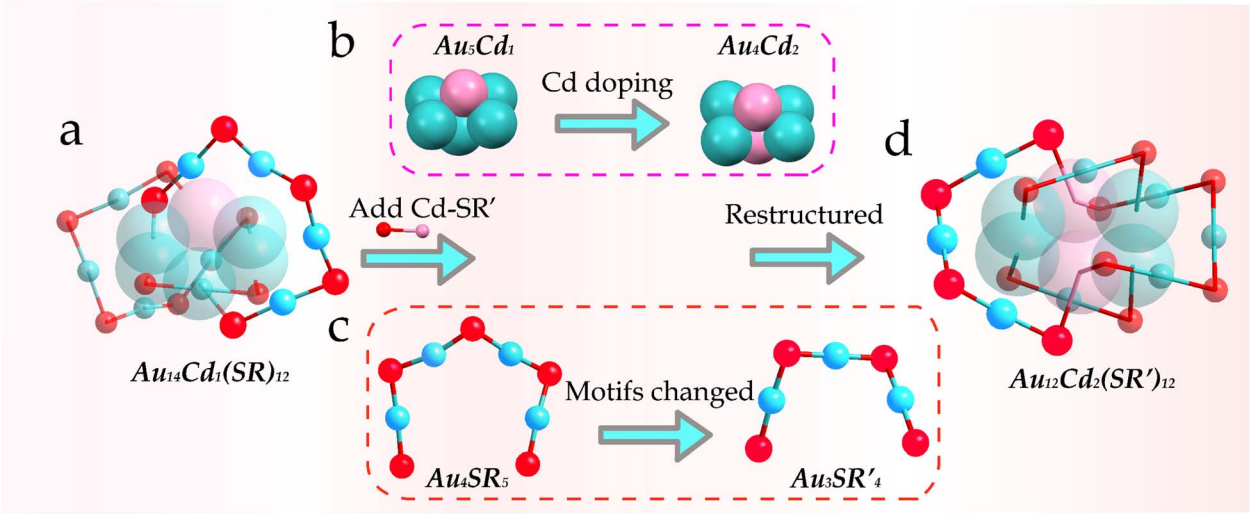

Fig. 3 Illustration of the transformation process from $Au_{14}Cd_1$ to $Au_{12}Cd_2$. (a) Overall structure of $Au_{14}Cd_1(SR)_{12}$; (b) the core of $Au_{14}Cd_1(SR)_{12}$ and that of $Au_{12}Cd_2(SR')_{12}$; (c) rearrangement of the motifs during transformation; (d) overall structure of $Au_{12}Cd_2(SR')_{12}$ (SR = 1-adamantasthiol, SR′ = *R*/*S*-fenchylthiol). (Color labels: blue = Au, pink = Cd, red = S, all the C and H atoms have been omitted for clarity).

performance. The fluorescence properties of the two clusters at different temperatures were further compared from 290 to 100 K. As shown in Fig. S26 and S27,† a gradual increase in the fluorescence intensity of the *R*/*L*-$Au_{12}Cd_2$ nanocluster was found when the temperature went down. This indicates that the fluorescence of the *R*/*L*-$Au_{12}Cd_2$ nanocluster is influenced by molecular rigidity, and the low temperature can limit the vibration of the molecules and thus enhance the fluorescence intensity of the nanocluster.[47] Based on the comparison of the temperature-dependent fluorescence spectra between $Au_{12}Cd_2$ and $Au_{14}Cd_1$, it can be found that from 290 to 100 K, as the ambient temperature decreases, the fluorescence intensities of $Au_{12}Cd_2$ and $Au_{14}Cd_1$ both increase (Fig. S26–S28†). However, at 100 K, the fluorescence intensity of $Au_{12}Cd_2$ is still significantly higher than that of $Au_{14}Cd_1$, indicating that the enhancement of fluorescence is mainly from the doping of the metal core but not the peripheral ligands, since reducing the temperature mainly affects the peripheral ligands rather than the inner core. On the other hand, more visible absorption peaks can be found with decreasing temperature, which indicates that the structure of the nanoclusters has not been destroyed and remains stable at low temperatures (Fig. S29–S31†).

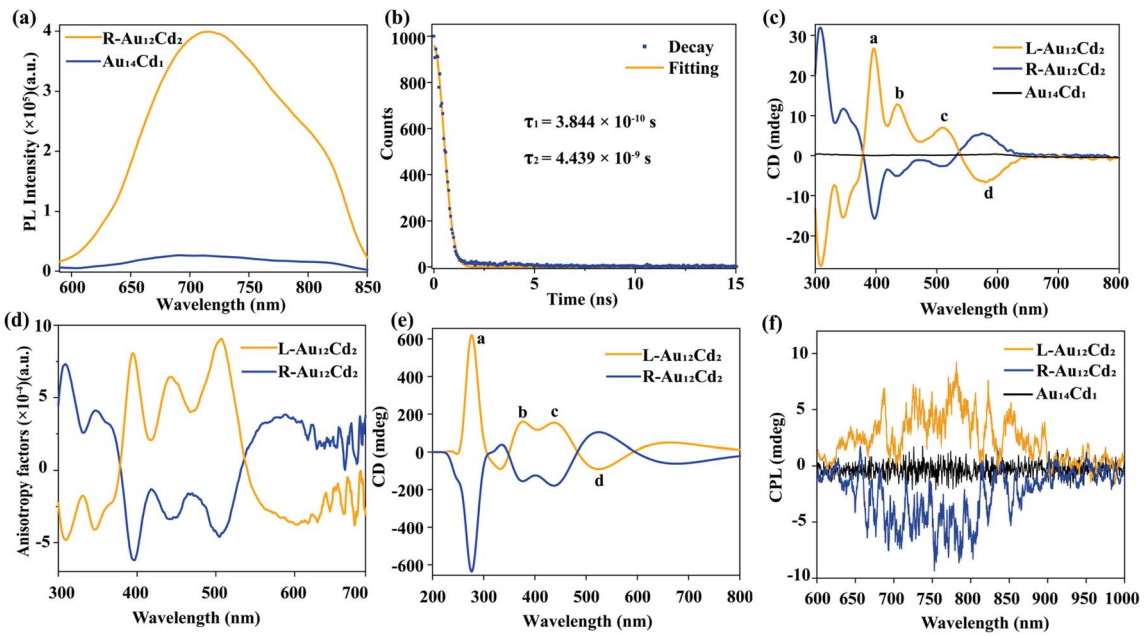

Fig. 4 (a) Comparison of the fluorescence intensity of *R*-$Au_{12}Cd_2$ and $Au_{14}Cd_1$; (b) fluorescence lifetime of the *R*-$Au_{12}Cd_2$ nanocluster; (c) circular dichroism spectra of *R*/*L*-$Au_{12}Cd_2$ and $Au_{14}Cd_1$; (d) the anisotropy factor (g_{abs}) of *L*-$Au_{12}Cd_2$ and *R*-$Au_{12}Cd_2$; (e) the calculated CD spectra of *L*-$Au_{12}Cd_2$ and *R*-$Au_{12}Cd_2$ nanoclusters; (f) circularly polarized luminescence spectra of *L*/*R*-$Au_{12}Cd_2$ and $Au_{14}Cd_1$.

To further explore the chiral properties of the $Au_{12}Cd_2$ nanocluster, circular dichroism (CD) tests were carried out. As shown in Fig. 4c, *L*-$Au_{12}Cd_2$ and *R*-$Au_{12}Cd_2$ show good mirror symmetry in their CD spectra, which showed a significant Cotton effect at a range from 300 to 650 nm, respectively. The maximum anisotropy factor value observed at 500 nm was found to reach 8×10^{-4} (Fig. 4d). In addition, the CD spectra of the *L*/*R*-fenchylthiol ligand are shown in Fig. S32,† in which the signals concentrated at around 300 nm, demonstrating that the signals of $Au_{12}Cd_2$ were derived from metal core and metal–ligand interfaces, indicating the transfer of chirality from the ligand to the core. This result is consistent with the analysis of the chiral origin supported by the geometric structure. That is, the chiral ligand can further induce distortion which results in the enhancement of their intrinsic chirality. To further investigate the origin of the CD spectral peaks, theoretical CD spectra of $Au_{12}Cd_2$ were calculated with the help of DFT. Comparison reveals that the theoretical and experimental CD spectra have a great similarity except a slight blueshift of the calculated peaks (Fig. 4e). In addition, the corresponding attributions of each peak are listed in the ESI (Fig. S33 and Table S7†).

The conversion of the cluster from $Au_{14}Cd_1$ to $Au_{12}Cd_2$ enhances not only the fluorescence but also the chiral properties, which suggests a possibility of producing the circularly polarized luminescence (CPL) properties. The CPL spectrophotometer was employed to examine the CPL properties of the *L*/*R* $Au_{12}Cd_2$ nanoclusters. As shown in Fig. 4f, a set of mirror symmetric circular polarization luminescence properties are displayed within the range from 600 to 1000 nm, which exactly corresponds to the position of photoluminescence. The maximum g_{lum} value was calculated to be 5.8×10^{-4} (Fig. S34†), which is similar to other nanoclusters (Table S8†). In addition, temperature-dependent CPL spectra revealed that the CPL intensity (Fig. S35†) and g_{lum} (Fig. S36†) of *R*/*L*-$Au_{12}Cd_2$ nanoclusters tend to increase with the decrease of temperature in the range from 290 to 100 K which was caused by the restriction of molecular motion at low temperature, and the relationship between the g_{lum} value and temperature can be described with an exponential decay function (Fig. S37†). Correspondingly, the DC curves of the *R*/*L*-$Au_{12}Cd_2$, which can reflect the fluorescence intensity of the sample, were also found to be enhanced with the decrease of temperature (Fig. S38†).

Conclusions

In this work, an $Au_{12}Cd_2$ nanocluster with CPL properties was obtained by simultaneously modulating the fluorescence and chirality of $Au_{14}Cd_1$ as the precursor. Time-dependent UV-vis spectra and thin-layer chromatograms revealed that the structural transformation from $Au_{14}Cd_1$ to $Au_{12}Cd_2$ was triggered by the thiol exchange and can be promoted with the addition of Cd atoms. X-ray crystallography revealed that the structural differences between $Au_{14}Cd_1$ and $Au_{12}Cd_2$ are mainly reflected in their surface motifs, while the alloying degree of the core was also improved. The increase of the core alloying has modulated the transition dipole moment of the clusters to enhance the fluorescence properties, and on the other hand, the induction of the peripheral rigid chiral ligands leads to the chiral distortion of the peripheral motifs, which endows them with optical activity. Finally, the circular polarization luminescence properties of $Au_{12}Cd_2$ were examined and the circularly polarized luminescence intensity was enhanced by limiting the molecular motion of the cluster. This work offers new insights into the construction of nanoclusters with CPL properties and lays the groundwork for more CPL-based applications.

Data availability

All the data supporting this article have been included in the main text and the ESI.†

Author contributions

J. Z. carried out the experiments, analyzed the data, and wrote the manuscript. X. Y. and P. Z. carried out the experiments. B. H. performed the calculations. Q. L. and J. C. revised the manuscript and assisted in the analysis. X. L. helped modify the language. M. Z. and S. Y. designed the project, analyzed the data, and revised the manuscript.

Conflicts of interest

There are no conflicts to declare.

Acknowledgements

The authors acknowledge financial support from the National Natural Science Foundation of China (21871001, 22001002, 22001003, 22301001), the Ministry of Education and the University Synergy Innovation Program of Anhui Province (GXXT-2020-053), the National Science Foundation of Anhui Province (2008085QB82, 2308085QB40), and the Innovation and Entrepreneurship Project of Returning Overseas Chinese Scholars in Anhui Province (2019LCX021).

Notes and references

1 I. Chakraborty and T. Pradeep, *Chem. Rev.*, 2017, **117**, 8208–8271.
2 X. Kang and M. Zhu, *Chem. Soc. Rev.*, 2019, **48**, 2422–2457.
3 Y. Zheng, L. Lai, W. Liu, H. Jiang and X. Wang, *Adv. Colloid Interface Sci.*, 2017, **242**, 1–16.
4 H. Yu, B. Rao, W. Jiang, S. Yang and M. Zhu, *Coord. Chem. Rev.*, 2019, **378**, 595–617.
5 Y. Chen, M. L. Phipps, J. H. Werner, S. Chakraborty and J. S. Martinez, *Acc. Chem. Res.*, 2018, **51**, 2756–2763.
6 T. Higaki, Q. Li, M. Zhou, S. Zhao, Y. Li, S. Li and R. Jin, *Acc. Chem. Res.*, 2018, **51**, 2764–2773.
7 Z. Wu, Q. Yao, S.-Q. Zang and J. Xie, *Natl. Sci. Rev.*, 2021, **8**, nwaa208.
8 X.-Y. Luo and M. Pan, *Coord. Chem. Rev.*, 2022, **468**, 214640.
9 Y. Zhang, S. Yu, B. Han, Y. Zhou, X. Zhang, X. Gao and Z. Tang, *Matter*, 2022, **5**, 837–875.

10 B. -C. Kim, H. -J. Choi, J. -J. Lee, F. Araoka and S. -W. Choi, *Adv. Funct. Mater.*, 2019, **29**, 1903246.
11 M. -M. Zhang, K. Li and S. -Q. Zang, *Adv. Opt. Mater.*, 2020, **8**, 1902152.
12 S. Wang, D. Hu, X. Guan, S. Cai, G. Shi, Z. Shuai, J. Zhang, Q. Peng and X. Wan, *Angew. Chem., Int. Ed.*, 2021, **60**, 21918–21926.
13 Y. Imai, Y. Nakano, T. Kawai and J. Yuasa, *Angew. Chem., Int. Ed.*, 2018, **130**, 9111–9116.
14 P. Reiné, J. Justicia, S. P. Morcillo, S. Abbate, B. Vaz, M. Ribagorda, Á. Orte, L. Á. Cienfuegos, G. Longhi, A. G. Campaña, D. Miguel and J. M. Cuerva, *J. Org. Chem.*, 2018, **83**, 4455–4463.
15 R. Hassey, E. J. Swain, N. I. Hammer, D. Venkataraman and M. D. Barnes, *Science*, 2006, **314**, 1437–1439.
16 J.-X. Gao, W.-Y. Zhang, Z.-G. Wu, Y.-X. Zheng and D.-W. Fu, *J. Am. Chem. Soc.*, 2020, **142**, 4756–4761.
17 Y. Yang, R. C. Costa, D.-M. Smilgies, A. J. Campbell and M. J. Fuchter, *Adv. Mater.*, 2013, **25**, 2624–2628.
18 X. Zhang, Y. Zhang, H. Zhang, Y. Quan, Y. Li, Y. Cheng and S. Ye, *Org. Lett.*, 2019, **21**, 439–443.
19 Y. Wu, C. Yan, X.-S. Li, L. H. You, Z.-Q. Yu, X. Wu, Z. Zheng, G. Liu, Z. Guo, H. Tian and W.-H. Zhu, *Angew. Chem., Int. Ed.*, 2021, **60**, 24549–24557.
20 C. Duan, B. Wang, J. Li, J. Xu, J. Zeng, J. Li, Z. Zhao, W. Gao, G. Ying and K. Chen, *Small*, 2022, **18**, 2204199.
21 X. Zhan, F.-F. Xu, Z. Zhou, Y. Yan, J. Yao and Y. Zhao, *Adv. Mater.*, 2021, **33**, 2104418.
22 W. Dai, Y. Wang, R. Li, Y. Fan, G. Qu, Y. Wu, Q. Song, J. Han and S. Xiao, *ACS Nano*, 2020, **14**, 17063–17070.
23 K. R. Krishnadas, L. Sementa, M. Medves, A. Fortunelli, M. Stener, A. Fürstenberg, G. Longhi and T. Bürgi, *ACS Nano*, 2020, **14**, 9687–9700.
24 H. Wu, X. He, B. Yang, C.-C. Li and L. Zhao, *Angew. Chem., Int. Ed.*, 2021, **60**, 1535–1539.
25 S. Li, Z.-P. Yan, X.-L. Li, Y.-J. Kong, H.-Y. Li, G.-G. Gao, Y.-X. Zheng and S.-Q. Zang, *Adv. Sci.*, 2020, **7**, 2000738.
26 S. Li, X.-Y. Dong, K.-S. Qi, S.-Q. Zang and T. C. W. Mak, *J. Am. Chem. Soc.*, 2021, **143**, 20574–20578.
27 L. Tang, A. Ma, C. Zhang, X. Liu, R. Jin and S. Wang, *Angew. Chem., Int. Ed.*, 2021, **60**, 17969–17973.
28 X. Kang, Y. Li, M. Zhu and R. Jin, *Chem. Soc. Rev.*, 2020, **49**, 6443–6514.
29 Q. Li, K. J. Lambright, M. G. Taylor, K. Kirschbaum, T.-Y. Luo, J. Zhao, G. Mpourmpakis, S. Mokashi-Punekar, N. L. Rosi and R. Jin, *J. Am. Chem. Soc.*, 2017, **139**, 17779–17782.
30 C. Yao, C.-Q. Xu, I.-H. Park, M. Zhao, Z. Zhu, J. Li, X. Hai, H. Fang, Y. Zhang, G. Macam, J. Teng, L. Li, Q.-H. Xu, F.-C. Chuang, J. Lu, C. Su, J. Li and J. Lu, *Angew. Chem., Int. Ed.*, 2020, **59**, 8270–8276.
31 W. Fei, S. Antonello, T. Dainese, A. Dolmella, M. Lahtinen, K. Rissanen, A. Venzo and F. Maran, *J. Am. Chem. Soc.*, 2019, **141**, 16033–16045.
32 S. Lee, M. S. Bootharaju, G. Deng, S. Malola, H. Häkkinen, N. Zheng and T. Hyeon, *J. Am. Chem. Soc.*, 2021, **143**, 12100–12107.
33 C. Zhu, J. Xin, J. Li, H. Li, X. Kang, Y. Pei and M. Zhu, *Angew. Chem., Int. Ed.*, 2022, **61**, e202205947.
34 X. Liu, G. Yao, X. Cheng, J. Xu, X. Cai, W. Hu, W. W. Xu, C. Zhang and Y. Zhu, *Chem. Sci.*, 2021, **12**, 3290–3294.
35 Y. Li, M. J. Cowan, M. Zhou, M. G. Taylor, H. Wang, Y. Song, M. Giannis and R. Jin, *ACS Nano*, 2020, **14**, 6599–6606.
36 Y. Liu, J. Zhang, B. Han, X. Wang, Z. Wang, C. Xue, G. Bian, D. Hu, R. Zhou, D.-S. Li, Z. Wang, Z. Ouyang, M. Li and T. Wu, *J. Am. Chem. Soc.*, 2020, **142**, 6649–6660.
37 M.-M. Zhang, X.-Y. Dong, Z.-Y. Wang, X.-M. Luo, J.-H. Huang, S.-Q. Zang and T. C. W. Mak, *J. Am. Chem. Soc.*, 2021, **143**, 6048–6053.
38 H. Yi, K. M. Osten, T. Levchenko, A. J. Veinot, Y. Aramaki, T. Ooi, M. Nambo and C. M. Crudden, *Chem. Sci.*, 2021, **12**, 10436–10440.
39 S. Yang, S. Chen, L. Xiong, C. Liu, H. Yu, S. Wang, N. L. Rosi, Y. Pei and M. Zhu, *J. Am. Chem. Soc.*, 2018, **140**, 10988–10994.
40 Q. Li, M. A. Mosquera, L. O. Jones, A. Parakh, J. Chai, R. Jin, G. C. Schatz and X. W. Gu, *ACS Nano*, 2020, **14**, 11888–11896.
41 Q. Li, D. Zhou, J. Chai, W. Y. So, T. Cai, M. Li, L. A. Peteanu, O. Chen, M. Cotlet, X. W. Gu, H. Zhu and R. Jin, *Nat. Commun.*, 2020, **11**, 2897.
42 F. Neese, *Wiley Comput. Mol. Sci.*, 2022, **12**, e1606.
43 J. P. Perdew, K. Burke and M. Ernzerhof, *Phys. Rev. Lett.*, 1996, **77**, 3865–3868.
44 J. P. Perdew, K. Burke and M. Ernzerhof, *Phys. Rev. Lett.*, 1997, **78**, 1396.
45 Y. Tan, Y. Lv, L. Xu, Q. Li, J. Chai, S. Yang, H. Yu and M. Zhu, *J. Am. Chem. Soc.*, 2023, **145**, 4238–4245.
46 J. Zhou, T. Li, Q. Li, P. Zheng, S. Yang, J. Chai and M. Zhu, *Inorg. Chem.*, 2022, **61**, 6493–6499.
47 D. Cortecchia, W. Mróz, S. Neutzner, T. Borzda, G. Folpini, R. Brescia and A. Petrozza, *Chem*, 2019, **5**, 2146–2158.